Magnetization dynamics in synthetic antiferromagnets with perpendicular magnetic anisotropy

Dingbin Huang [1,*] Delin Zhang [2] Yun Kim [1] Jian-Ping Wang [2] and Xiaojia Wang [1,†]
[1]*Department of Mechanical Engineering, University of Minnesota, Minneapolis, Minnesota 55455, USA*
[2]*Department of Electrical and Computer Engineering, University of Minnesota, Minneapolis, Minnesota 55455, USA*

(Received 21 October 2022; revised 8 May 2023; accepted 6 June 2023; published 26 June 2023)

Understanding the rich physics of magnetization dynamics in perpendicular synthetic antiferromagnets (p-SAFs) is crucial for developing next-generation spintronic devices. In this work, we systematically investigate the magnetization dynamics in p-SAFs combining time-resolved magneto-optical Kerr effect (TR-MOKE) measurements with theoretical modeling. These model analyses, based on a Landau-Lifshitz-Gilbert approach incorporating exchange coupling, provide details about the magnetization dynamic characteristics including the amplitudes, directions, and phases of the precession of p-SAFs under varying magnetic fields. These model-predicted characteristics are in excellent quantitative agreement with TR-MOKE measurements on an asymmetric p-SAF. We further reveal the damping mechanisms of two precession modes coexisting in the p-SAF and successfully identify individual contributions from different sources, including Gilbert damping of each ferromagnetic layer, spin pumping, and inhomogeneous broadening. Such a comprehensive understanding of magnetization dynamics in p-SAFs, obtained by integrating high-fidelity TR-MOKE measurements and theoretical modeling, can guide the design of p-SAF-based architectures for spintronic applications.

DOI: 10.1103/PhysRevB.107.214438

I. INTRODUCTION

Synthetic antiferromagnetic (SAF) structures have attracted considerable interest for applications in spin memory and logic devices because of their unique magnetic configurations [1–3]. The SAF structures are composed of two ferromagnetic (FM) layers antiparallelly coupled through a nonmagnetic (NM) spacer, offering great flexibilities for the manipulation of magnetic configurations through external stimuli (e.g., electric-field and spin-orbit torque, SOT). This permits the design of new architectures for spintronic applications, such as magnetic tunnel junction (MTJ), SOT devices, domain wall devices, skyrmion devices, among others [4–7]. The SAF structures possess many advantages for such applications, including fast switching speeds (potentially in the THz regimes), low offset fields, small switching currents (and thus low energy consumption), high thermal stability, excellent resilience to perturbations from external magnetic fields, and large turnability of magnetic properties [3,8–16].

A comprehensive study of the magnetization dynamics of SAF structures can facilitate the understanding of the switching behavior of spintronic devices, and ultimately guide the design of novel device architectures. Different from a single FM free layer, magnetization dynamics of the SAF structures involves two modes of precession, namely high-frequency (HF) and low-frequency (LF) modes, that result from the hybridization of magnetizations precession in the two FM layers. The relative phase and precession amplitude in two FM layers can significantly affect the spin-pumping enhancement of magnetic damping [17], and thus play an important role in determining the magnetization dynamic behaviors in SAFs. Heretofore, the exchange-coupling strength and magnetic damping constant of SAFs have been studied by ferromagnetic resonance (FMR) [18–21] and optical metrology [22–25]. Most FMR-based experimental studies were limited to SAFs with in-plane magnetic anisotropy. For device applications, perpendicular magnetic anisotropy (PMA) gives better scalability [3,26]. Therefore, the characteristics of magnetization dynamics of perpendicular SAF (p-SAF) structures are of much value to investigate. In addition, prior studies mainly focused on the mutual spin pumping between two FM layers [22,27,28]. A more thorough understanding of the contributions from various sources, including inhomogeneous broadening [29], remains elusive.

In this paper, we report a comprehensive study of the magnetization dynamics of p-SAFs by integrating high-fidelity experiments and theoretical modeling to detail the characteristic parameters. These parameters describe the amplitude, phase, and direction of magnetization precession of both the HF and LF modes for the two exchange-coupled FM layers in a p-SAF. We conduct all-optical time-resolved magneto-optical Kerr effect (TR-MOKE) measurements [30–33] on an asymmetric p-SAF structure with two different FM layers. The field-dependent amplitude and phase of TR-MOKE signals can be well captured by our theoretical model, which in turn provides comprehensive physical insights into the magnetization dynamics of p-SAF structures. Most importantly, we show that inhomogeneous broadening plays a critical role in determining the effective damping of both HF and LF modes, especially at low fields. We demonstrate the quantification of contributions from inhomogeneous broadening and mutual spin pumping (i.e., the exchange of angular

*Corresponding author: huan1746@umn.edu
†Corresponding author: wang4940@umn.edu

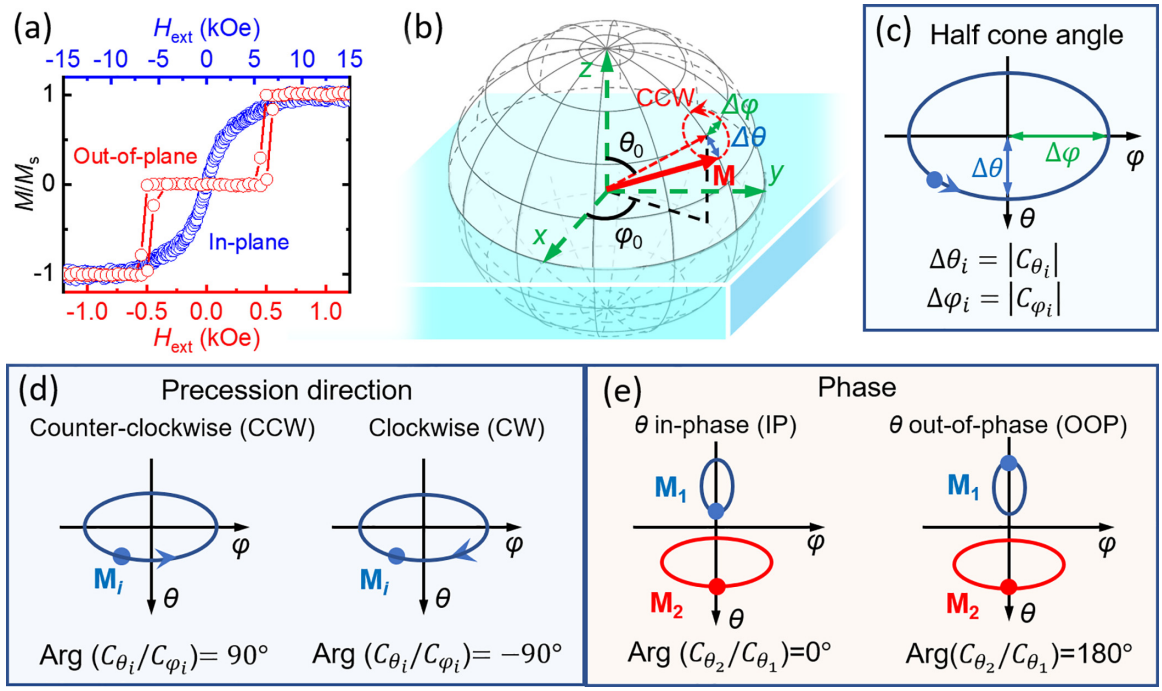

FIG. 1. (a) Magnetic hysteresis (M-H_{ext}) loops of the p-SAF stack. The magnetization is normalized to the saturation magnetization (M/M_s). (b) Schematic illustration of the half cone angles ($\Delta\theta$ and $\Delta\varphi$) and precession direction of magnetization. The precession direction is defined from a view against the equilibrium direction (θ_0, φ_0) of **M**. The representative precession direction in the schematic is counterclockwise (CCW). (c) The relation between precession half cone angles and the prefactors. (d) The relation between precession direction and the prefactors. (e) The relative phase between two FM layers for different prefactor values.

momentum between two FM layers via pumped spin currents) [21] to the effective damping, enabling accurate determination of the Gilbert damping for individual FM layers. The results of this work are beneficial for designing p-SAF-based architectures in spintronic applications. Additionally, this work also serves as a successful example demonstrating that TR-MOKE, as an all-optical metrology, is a powerful tool to capture the magnetization dynamics and reveal the rich physics of complex structures that involve multilayer coupling.

II. METHODOLOGY

A. Sample preparation and characterization

One SAF structure was deposited onto thermally oxidized silicon wafers with a 300-nm SiO_2 layer by magnetron sputtering at room temperature in a six-target ultrahigh vacuum Shamrock sputtering system. The base pressure is below 5×10^{-8} Torr. The stacking structure of the SAF is: $[Si/SiO_2]_{sub}/[Ta(5)/Pd(3)]_{seed}/[Co(0.4)/Pd(0.7)/Co(0.4)]_{FM1}/[Ru(0.6)/Ta(0.3)]_{NM}/CoFeB(1)_{FM2}/[MgO(2)/Ta(3)]_{capping}$. The numbers in parentheses denote the layer thicknesses in nanometers. After deposition, the sample was annealed at 250 °C for 20 minutes by a rapid-thermal-annealing process. The two FM layers are CoFeB and Co/Pd/Co layers, separated by a Ru/Ta spacer, forming an asymmetric p-SAF structure (i.e., two FM layers having different magnetic properties). The M-H_{ext} loops were characterized by a physical property measurement system with a vibrating-sample magnetometer module. The resulting M-H_{ext} loops are displayed in Fig. 1(a). Under low out-of-plane fields ($H_{ext} < 500$ Oe), the total magnetic moments in two FM layers of the SAF stack perfectly cancel out each other: $M_1 d_1 = M_2 d_2$ with M_i and d_i being the magnetization and thickness of each FM layer ($i = 1$ for the top CoFeB layer and $i = 2$ for the bottom Co/Pd/Co layer). The spin-flipping field ($H_f \approx 500$ Oe) in the out-of-plane loop indicates the bilinear interlayer-exchange-coupling (IEC) J_1 between the two FM layers: $J_1 = -H_f M_{s,1} d_1 \approx -0.062$ erg cm^{-2} [34]. The values of $M_{s,1}$, $M_{s,2}$, d_1, and d_2 can be found in Table SI of the Supplemental Material (SM) [35].

B. Theoretical foundation of magnetization dynamics for a p-SAF structure

The magnetic free energy per unit area for a p-SAF structure with uniaxial PMA can be expressed as [36]

$$F = -J_1(\mathbf{m}_1 \cdot \mathbf{m}_2) - J_2(\mathbf{m}_1 \cdot \mathbf{m}_2)^2 + \sum_{i=1}^{2} d_i M_{s,i}\left[-\frac{1}{2}H_{k,\mathrm{eff},i}(\mathbf{n} \cdot \mathbf{m}_i)^2 - \mathbf{m}_i \cdot \mathbf{H}_{ext}\right], \quad (1)$$

where J_1 and J_2 are the strength of the bilinear and biquadratic IEC. $\mathbf{m}_i = \mathbf{M}_i/M_{s,i}$ are the normalized magnetization vectors for individual FM layers ($i = 1, 2$). d_i, $M_{s,i}$, and $H_{k,\mathrm{eff},i}$ denote, respectively, the thickness, saturation magnetization, and the effective anisotropy field of the ith layer. **n** is a unit vector indicating the surface normal direction of the film. For the convenience of derivation and discussion, the direction of $\mathbf{m}_i$ is represented in the spherical coordinates by the polar angle θ_i and the azimuthal angle φ_i, as shown in Fig. 1(b).

The equilibrium direction of magnetization in each layer $(\theta_{0,i}, \varphi_{0,i})$ under a given $\mathbf{H}_{\text{ext}}$ is obtained by minimizing F in the $(\theta_1, \varphi_1, \theta_2, \varphi_2)$ space. The magnetization precession is governed by the Landau-Lifshitz-Gilbert (LLG) equation considering the mutual spin pumping between two FM layers [27,37–40]:

$$\frac{d\mathbf{M}_i}{dt} = -\gamma_i \mathbf{M}_i \times \mathbf{H}_{\text{eff},i} + \frac{(\alpha_{0,i} + \alpha_{\text{sp},ii})}{M_{\text{s},i}} \mathbf{M}_i \times \frac{d\mathbf{M}_i}{dt} - \frac{\alpha_{\text{sp},ij}}{M_{\text{s},i}} \mathbf{M}_i \times \left(\mathbf{m}_j \times \frac{d\mathbf{m}_j}{dt} \right) \times \mathbf{M}_i. \quad (2)$$

On the right-hand side of Eq. (2), the first term describes the precession with the effective field $\mathbf{H}_{\text{eff},i}$ in each layer, given by the partial derivative of the total free energy in the $\mathbf{M}$ space via $\mathbf{H}_{\text{eff},i} = -\nabla_{\mathbf{M}_i} F$. The second term represents the relaxation induced by Gilbert damping (α) of the ith layer, which includes the intrinsic $(\alpha_{0,i})$ and spin-pumping-enhanced $(\alpha_{\text{sp},ii})$ damping. For TR-MOKE measurements, $\alpha_{0,i}$ and $\alpha_{\text{sp},ii}$ are indistinguishable. Hence, we define $\alpha_i = \alpha_{0,i} + \alpha_{\text{sp},ii}$ to include both terms. The last term in Eq. (2) considers the influence of pumped spin currents from the layer j on the magnetization dynamics of the layer i.

The time evolution of $\mathbf{M}_i$ can be obtained by solving the linearized Eq. (2). Details are provided in Note 1 of the SM [35]. The solutions to Eq. (2) in spherical coordinates are

$$\begin{aligned} \begin{bmatrix} \theta_1(t) \\ \varphi_1(t) \\ \theta_2(t) \\ \varphi_2(t) \end{bmatrix} &= \begin{bmatrix} \theta_{0,1} \\ \varphi_{0,1} \\ \theta_{0,2} \\ \varphi_{0,2} \end{bmatrix} + \begin{bmatrix} \Delta\theta_1(t) \\ \Delta\varphi_1(t) \\ \Delta\theta_2(t) \\ \Delta\varphi_2(t) \end{bmatrix} \\ &= \begin{bmatrix} \theta_{0,1} \\ \varphi_{0,1} \\ \theta_{0,2} \\ \varphi_{0,2} \end{bmatrix} + \begin{bmatrix} C_{\theta,1}^{\text{HF}} \\ C_{\varphi,1}^{\text{HF}} \\ C_{\theta,2}^{\text{HF}} \\ C_{\varphi,2}^{\text{HF}} \end{bmatrix} \exp(i\omega^{\text{HF}} t) \\ &\quad + \begin{bmatrix} C_{\theta,1}^{\text{LF}} \\ C_{\varphi,1}^{\text{LF}} \\ C_{\theta,2}^{\text{LF}} \\ C_{\varphi,2}^{\text{LF}} \end{bmatrix} \exp(i\omega^{\text{LF}} t) \end{aligned} \quad (3)$$

with $\Delta\theta_i$ and $\Delta\varphi_i$ representing the deviation angles of magnetization from its equilibrium direction along the polar and azimuthal directions. The last two terms are the linear combination of two eigen-solutions, denoted by superscripts HF (high-frequency mode) and LF (low-frequency mode). ω is the complex angular frequencies of two modes, with the real and imaginary parts representing the precession angular frequency $(f/2\pi)$ and relaxation rate $(1/\tau)$, respectively. For each mode, the complex prefactor vector $[C_{\theta,1}, C_{\varphi,1}, C_{\theta,2}, C_{\varphi,2}]^T$ contains detailed information about the magnetization dynamics. As illustrated in Fig. 1(c), the moduli, $|C_{\theta,i}|$ and $|C_{\varphi,i}|$ correspond to the half cone angles of the precession in layer i along the polar and azimuthal directions for a given mode immediately after laser heating, as shown by $\Delta\theta$ and $\Delta\varphi$ in Figs. 1(b) and 1(c). The phase difference between $\Delta\theta_i$ and $\Delta\varphi_i$, defined as $\text{Arg}(\Delta\theta_i/\Delta\varphi_i) = \text{Arg}(C_{\theta,i}/C_{\varphi,i})$ with Arg representing the argument of complex numbers, determines the direction of precession. If $\Delta\theta_i$ advances $\Delta\varphi_i$ by 90°, meaning $\text{Arg}(C_{\theta,i}/C_{\varphi,i}) = 90°$, the precession is counterclockwise (CCW) in the θ-φ space (from a view against $\mathbf{M}_i$). $\text{Arg}(C_{\theta,i}/C_{\varphi,i}) = -90°$, on the contrary, suggests clockwise (CW) precession [Fig. 1(d)]. Further, the argument of $C_{\theta,2}/C_{\theta,1}$ provides the relative phase in two FM layers. $\text{Arg}(C_{\theta,2}/C_{\theta,1}) = 0°$ corresponds to the precession motions in two FM layers that are in-phase (IP) in terms of θ for a given mode. While the out-of-phase (OOP) precession in terms of θ is represented by $\text{Arg}(C_{\theta,2}/C_{\theta,1}) = 180°$ [Fig. 1(e)]. Given the precession direction in each layer and the phase difference between the two FM layers in terms of θ, the phase difference in terms of φ can be automatically determined.

As for the effective damping $\alpha_{\text{eff}} = 1/2\pi f\tau$, in addition to the intrinsic damping $(\alpha_{0,i})$ and the spin-pumping contribution $(\alpha_{\text{sp},ii}$ and $\alpha_{\text{sp},ji})$ considered in Eq. (2), inhomogeneities can also bring substantial damping enhancement [32,33,41,42]. Here, we model the total relaxation rate as follows:

$$\frac{1}{\tau^{\Phi}} = -\text{Im}(\omega^{\Phi}) + \frac{1}{\tau_{\text{inhomo}}^{\Phi}}. \quad (4)$$

The superscript $\Phi = \text{HF}$ or LF, representing either the high-frequency or low-frequency precession modes. ω^{Φ} includes both the intrinsic and spin-pumping contributions. The inhomogeneous broadening is calculated as

$$\frac{1}{\tau_{\text{inhomo}}^{\Phi}} = \sum_i \frac{1}{\pi} \left| \frac{\partial f^{\Phi}}{\partial H_{\text{k,eff},i}} \right| \Delta H_{\text{k,eff},i} + \sum_i \frac{1}{\pi} \left| \frac{\partial f^{\Phi}}{\partial J_i} \right| \Delta J_i, \quad (5)$$

where the first summation represents the contribution from the spatial variation of the effective anisotropy field of individual FM layers $(\Delta H_{\text{k,eff},i})$. The second summation denotes the contribution from the spatial fluctuations of the bilinear and biquadratic IEC (ΔJ_1 and ΔJ_2). According to Slonczewski's "thickness fluctuations" theory, ΔJ_1 generates J_2 [43,44]. Therefore, the fact that $J_2 = 0$ for our sample suggests that ΔJ_1 is sufficiently small, allowing us to neglect the inhomogeneous broadening from the fluctuations of both the bilinear and biquadratic IEC in the following analyses.

C. Detection of magnetization dynamics

The magnetization dynamics of the p-SAF sample is detected by TR-MOKE, which is ultrafast-laser-based metrology utilizing a pump-probe configuration. In TR-MOKE, pump laser pulses interact with the sample, initiating magnetization dynamics in magnetic layers via inducing ultrafast thermal demagnetization. The laser-induced heating brings a rapid decrease to the magnetic anisotropy fields and IEC [45,46], which changes $\theta_{0,i}$, $\varphi_{0,i}$ and initiates the precession. The magnetization dynamics due to pump excitation is detected by a probe beam through MOKE. In our setup, the incident probe beam is normal to the sample surface (polar MOKE); therefore, the Kerr rotation angle (θ_{K}) of the reflected probe beam is proportional to the z component of the magnetization [47]. More details about the experimental setup can be found in Refs. [30,32]. For p-SAF, TR-MOKE signals contain two oscillating frequencies that correspond to the HF and LF modes $(f^{\text{HF}} > f^{\text{LF}})$. The signals are proportional to

the change in θ_K and can be analyzed as follows:

$$\Delta\theta_K(t) = A + Be^{-t/\tau^T} + C^{HF}\cos(2\pi f^{HF}t + \beta^{HF})e^{-\frac{t}{\tau^{HF}}} + C^{LF}\cos(2\pi f^{LF}t + \beta^{LF})e^{-\frac{t}{\tau^{LF}}}, \quad (6)$$

where the exponential term Be^{-t/τ^T} is related to the thermal background with τ^T being the time scale of heat dissipation. The rest two terms on the right-hand side are the precession terms with C, f, β, and τ denoting, respectively, the amplitude, frequency, phase, and relaxation time of the HF and LF modes.

After excluding the thermal background from TR-MOKE signals, the precession is modeled with the initial conditions of step-function decreases in $H_{k,eff,i}$ and J_i, following the ultrafast laser excitation [48]. This is a reasonable approximation since the precession period ($\sim$15 − 100 ps for H_{ext} > 5 kOe) is much longer than the time scales of the laser excitation ($\sim$1.5 ps) and subsequent relaxations among electrons, magnons, and lattice ($\sim$1 − 2 ps) [49], but much shorter than the time scale of heat dissipation-governed recovery ($\sim$400 ps). With these initial conditions, the prefactors in Eq. (3) can be determined (see more details in Note 1 of the SM [35]).

For our SAF structure, θ_K detected by the probe beam contains weighted contributions from both the top and bottom FM layers:

$$\frac{\theta_K(t)}{\theta_{K,s}} = w\cos\theta_1(t) + (1-w)\cos\theta_2(t), \quad (7)$$

where $\theta_{K,s}$ represents the Kerr rotation angle when the SAF stack is saturated along the positive out-of-plane (z) direction. w is the weighting factor, considering the different contributions to the total MOKE signals from two FM layers. w can be obtained from static MOKE measurements [50], which gives $w = 0.457$ (see more details in Note 2 of the SM [35]).

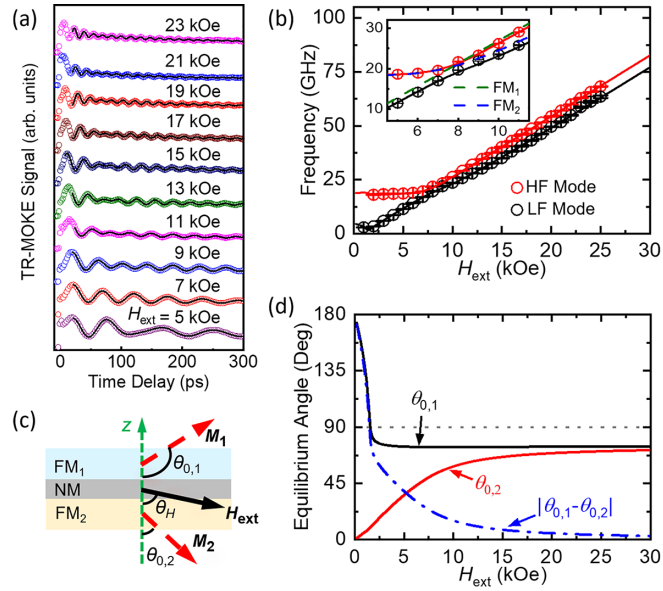

FIG. 2. (a) TR-MOKE signals under varying H_{ext} when θ_H = 75° [as defined in (c)]. Circles are the experimental data and black lines are the fitting curves based on Eq. (6). (b) The precession frequencies of the HF and LF modes as functions of H_{ext}. Circles are experimental data and solid lines are fitting curves. The inset highlights the zoomed-in view of the field-dependent frequencies around 8 kOe, where the green dashed line and blue dashed line are the single-layer (SL) precession frequencies of FM_1 and FM_2 without interlayer exchange coupling. (c) Schematic illustration of the definition of the equilibrium polar angles ($\theta_{0,1}$ and $\theta_{0,2}$), and the direction of the external magnetic field (θ_H). The illustration is equivalent to Fig. 1(b) due to symmetry. (d) $\theta_{0,1}$ and $\theta_{0,2}$ as functions of H_{ext}. The dashed-dotted line plots the difference between the two equilibrium polar angles.

III. RESULTS AND DISCUSSION

A. Field-dependent precession frequencies and equilibrium magnetization directions

TR-MOKE signals measured at varying H_{ext} are depicted in Fig. 2(a). The external field is tilted 15° away from in-plane [θ_H = 75°, as defined by Fig. 2(c)] to achieve larger amplitudes of TR-MOKE signals [51]. The signals can be fitted to Eq. (6) to extract the LF and HF precession modes. The field-dependent precession frequencies of both modes are summarized in Fig. 2(b). For simplicity, when analyzing precession frequencies, magnetic damping and mutual spin pumping are neglected due to its insignificant impacts on precession frequencies. By comparing the experimental data and the prediction of $\omega^{HF}/2\pi$ and $\omega^{LF}/2\pi$ based on Eq. (3), the effective anisotropy fields and the IEC strength are fitted as $H_{k,eff,1} = 1.23 \pm 0.28$ kOe, $H_{k,eff,2} = 6.18 \pm 0.13$ kOe, $J_1 = -0.050 \pm 0.020$ erg cm^{-2}, and $J_2 = 0$. All parameters and their determination methods are summarized in Table SI of the SM [35]. The fitted J_1 is close to that obtained from the M-H_{ext} loops (~ -0.062 erg cm^{-2}). The inset of Fig. 2(b) shows the zoomed-in view of field-dependent precession frequencies around H_{ext} = 8 kOe, where an anticrossing feature is observed: a narrow gap ($\sim$2 GHz) opens in the frequency dispersion curves of the HF and LF modes owing to the weak IEC between two FM layers. Without any IEC, the precession frequencies of two FM layers would cross at H_{ext} = 8 kOe, as indicated by the green dashed line and blue dashed line in the figure. We refer to these two sets of crossing frequencies as the single-layer natural frequencies of two FM layers (FM_1 and FM_2) in the following discussions.

Based on the fitted stack properties ($H_{k,eff,1}$, $H_{k,eff,2}$, J_1, and J_2), the equilibrium magnetization directions in the two layers can be calculated. For SAFs with weak IEC compared with uniaxial PMA, the azimuthal angles of the magnetization in two FM layers are always the same as that of the external field at equilibrium status. Therefore, two polar angles will be sufficient to describe the equilibrium magnetization configuration. Figure 2(c) illustrates the definition of the equilibrium polar angles of two FM layers ($\theta_{0,1}$, $\theta_{0,2}$) and the external field (θ_H). The values of $\theta_{0,1}$, $\theta_{0,2}$, and the difference between these two polar angles as functions of H_{ext} are shown in Fig. 2(d). When H_{ext} is low (<1.6 kOe), magnetic anisotropy and antiferromagnetic coupling are dominant and $|\theta_{0,1} - \theta_{0,2}|$ is larger than 90°. As H_{ext} increases, both $\theta_{0,1}$ and $\theta_{0,2}$ approach θ_H. When H_{ext} is high (>15 kOe), the Zeeman energy becomes dominant and both M_1 and M_2 are almost aligned with H_{ext}.

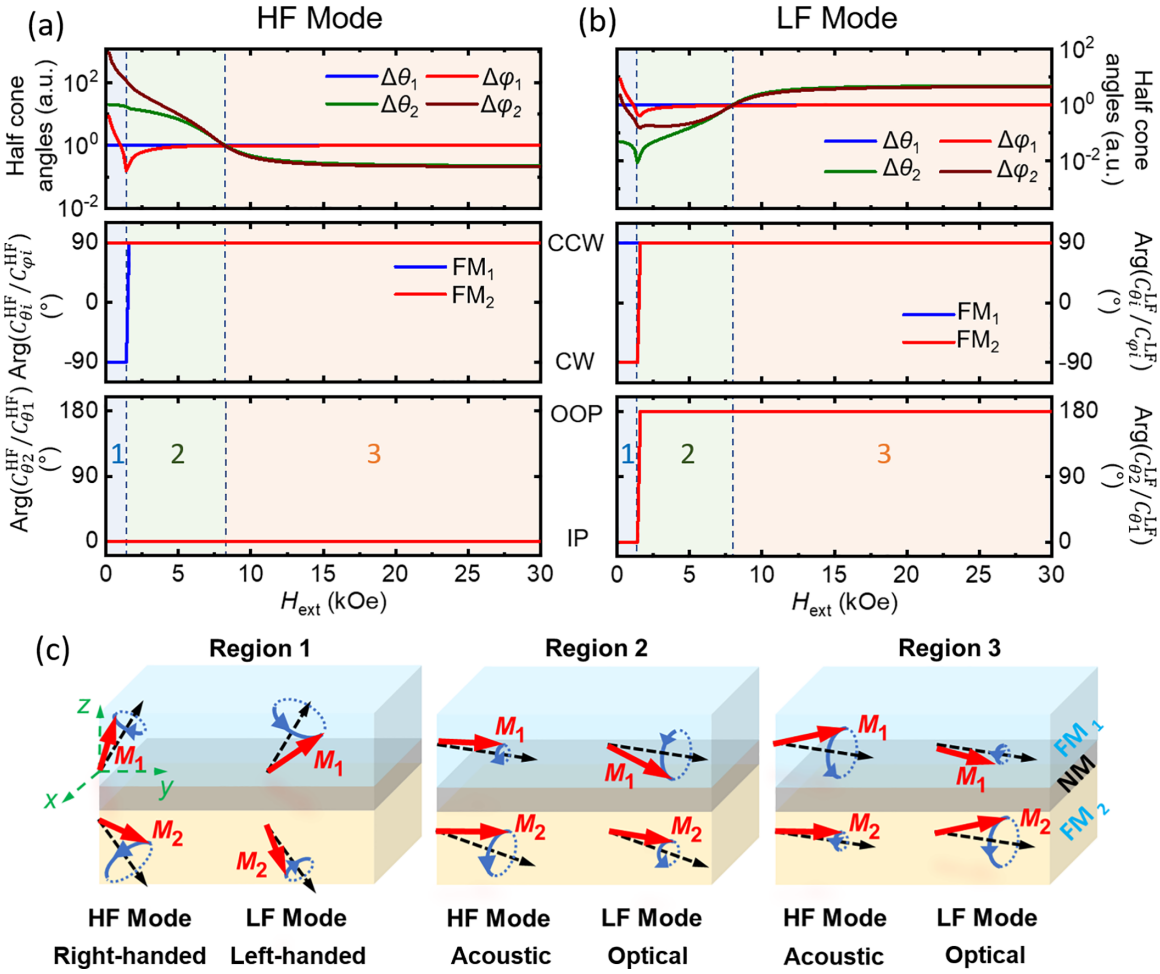

FIG. 3. The calculated half cone angle, direction, and phase of magnetization precession for (a) the HF mode and (b) the LF mode. In the top row, four curves represent the polar and azimuthal half cone angles of precession in two FM layers. All half cone angles are normalized with respect to $\Delta\theta_1$. The middle row shows the value of $\mathrm{Arg}(C_{\theta,i}/C_{\varphi,i})$ under different H_{ext}. A value of 90° (−90°) represents CCW (CW) precession. The bottom row is the phase difference of the polar angles in two layers. A value of 0° (180°) corresponds to the polar angles of the magnetization in two layers are IP (OOP) during precession. Dashed lines correspond to the reference case where damping is zero in both layers. (c) Schematic illustrations of the cone angle, direction, and phase of magnetization precession for the HF and LF modes in different regions, and their corresponding characteristics regarding chirality and phase difference.

B. Cone angle, direction, and phase of magnetization precession revealed by modeling

Besides the equilibrium configuration, using sample properties extracted from Fig. 2(b) as input parameters, the LLG-based modeling (described in Sec. II B) also provides information on the cone angle, direction, and phase of magnetization precession for each mode (Fig. 1). The discussion in this section is limited to the case without damping and mutual spin pumping. They will be considered in Note 4 of the SM [35], Secs. 3.3, and 3.4. The calculation results are shown in Fig. 3, which are categorized into three regions. At high external fields ($H_{\mathrm{ext}} > 1.6$ kOe, regions 2 and 3), both FM layers precess CCW [$\mathrm{Arg}(C_{\theta,i}/C_{\varphi,i}) = 90°$], and the polar angles of magnetization in two layers are IP [$\mathrm{Arg}(C_{\theta,2}/C_{\theta,1}) = 0°$] for the HF mode and OOP [$\mathrm{Arg}(C_{\theta,2}/C_{\theta,1}) = 180°$] for the LF mode. This is the reason for the HF mode (LF mode) also being called the acoustic mode (optical mode) in the literature [23]. The criterion to differentiate region 2 from region 3 is the FM layer that dominates a given precessional mode (i.e., the layer with larger precession cone angles). In region 2 (1.6 kOe $< H_{\mathrm{ext}} <$ 8 kOe), the HF mode is dominated by FM_2 because FM_2 has larger cone angles than FM_1. This is reasonable since the higher precession frequency is closer to the natural frequency of FM_2 [see Fig. 2(b)] in region 2. Similarly, in region 3, the HF mode is dominated by FM_1 with larger precession cone angles.

When H_{ext} is low (region 1), the angle between two magnetizations is larger than 90° [Fig. 2(d)] owing to the more dominant AF-exchange-coupling energy as compared with the Zeeman energy. In this region, magnetization dynamics exhibits some unique features. Firstly, CW [$\mathrm{Arg}(C_{\theta,i}/C_{\varphi,i}) = -90°$] precession emerges: for each mode, the dominant layer precesses CCW (FM_2 for the HF mode and FM_1 for the LF mode) and the subservient layer precesses CW (FM_1 for the HF mode and FM_2 for the LF mode). This is because the effective field for the subservient layer [e.g., $\mathbf{H}_{\mathrm{eff},1}$ for the HF mode, see Eq. (2)] precesses CW owing to the CCW precession of the dominant layer when $|\theta_{0,1} - \theta_{0,2}| >$

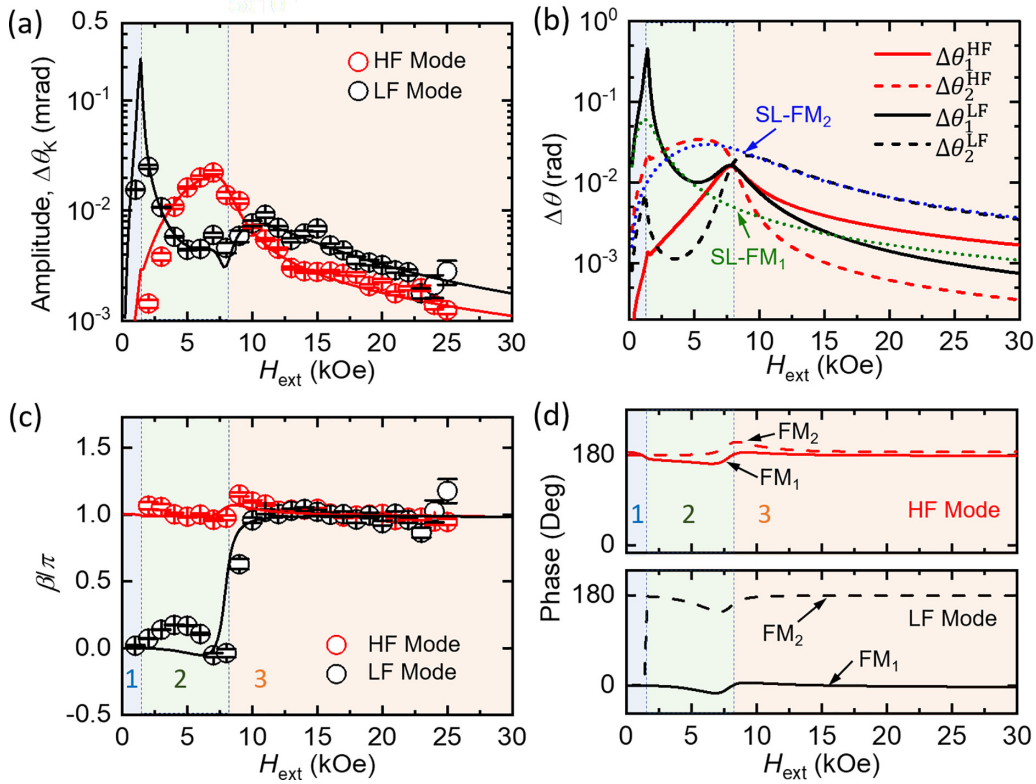

FIG. 4. (a) Amplitudes of TR-MOKE signals as functions of H_{ext}. The circles and curves represent experimental data and modeling fitting, respectively. (b) The calculated precession half cone angles at different H_{ext}. Red curves and black curves represent the cone angles of the HF mode and the LF mode in FM_1 (solid lines) and FM_2 (dashed lines). Dotted lines are the precession cone angles of single-layer (SL) FM_1 and FM_2 without IEC. (c) Phases of TR-MOKE signals at varying H_{ext}. Circles and curves are experimental data and modeling fitting ($\alpha_{sp,12} = 0.010$, $\alpha_{sp,21} = 0.007$, $\alpha_1 = 0.020$, $\alpha_2 = 0.060$). (d) Simulated precession phase of the HF mode (red curves) and the LF mode (black curves) in FM_1 (solid lines) and FM_2 (dashed lines).

90° [Fig. 2(d)]. In other words, a low H_{ext} that makes $|\theta_{0,1} - \theta_{0,2}| > 90°$ is a necessary condition for the CW precession. However, it is not a sufficient condition. In general, certain degrees of symmetry breaking ($H_{k,eff,1} \neq H_{k,eff,2}$ or the field is tilted away from the direction normal to the easy axis) are also needed to generate CW precession. For example, for symmetric antiferromagnets ($H_{k,eff,1} = H_{k,eff,2}$) under fields perpendicular to the easy axis, CW precession does not appear even at low fields (Fig. 2(a) in Ref. [52]). See Note 5 of the SM [35] for more details. Secondly, as shown in Fig. 3, the precession motions in two FM layers are always IP for both HF and LF modes; thus, there is no longer a clear differentiation between "acoustic mode" and "optical mode". Instead, the two modes can be differentiated as "right-handed" and "left-handed" based on the chirality [53]. Here, we define the chirality with respect to a reference direction taken as the projection of H_{ext} or $\mathbf{M}_2$ (magnetization direction of the layer with a higher $H_{k,eff}$) on the easy axis [$-z$ direction in Fig. 3(c)]. Lastly, the shape of the precession cone also varies in different regions. $\Delta\theta_i$ and $\Delta\varphi_i$ are almost the same for both modes in region 3, indicating the precession trajectories are nearly circular. While in regions 1 and 2, $\Delta\theta_i$ and $\Delta\varphi_i$ are not always equal, suggesting the precession trajectories may have high ellipticities.

C. Amplitude and phase of TR-MOKE signals

Actual magnetization dynamics is resolvable as a linear combination of the two eigenmodes (the HF and the LF modes). By taking into account the initial conditions (i.e., laser excitation, see Note 1 of the SM [35]), we can determine the amplitude and phase of the two modes in TR-MOKE signals. Figure 4(a) summarizes the amplitudes of both HF and LF modes [C^{HF} and C^{LF} in Eq. (3)] under different H_{ext}. Noted that the y axis represents Kerr angle (θ_K) instead of the cone angle of precession. The LF mode has a local minimum near 8 kOe, where the two FM layers have similar precession cone angles but opposite phases for the LF mode [Fig. 3(b)]. The amplitudes of both modes decrease with H_{ext} in the high-field region. This is similar to the single-layer case, where the amplitudes of TR-MOKE signals decrease with H_{ext} because the decrease in $H_{k,eff}$ induced by laser heating is not able to significantly alternate the equilibrium magnetization direction when the Zeeman energy dominates [51]. The LF mode also has an amplitude peak at low fields ($H_{ext} < 3$ kOe), where the dominant layer of FM_1 changes its equilibrium direction dramatically with H_{ext} (from ~75° to 170°) as shown in Fig. 2(d).

To directly compare the amplitudes of TR-MOKE signals and the LLG-based calculations, the weighting factor w and the initial conditions are needed. The initial conditions

are determined by $H'_{k,eff,1}$, $H'_{k,eff,2}$, and J'_1, representing the instantaneous effective anisotropy fields and IEC strength upon laser heating. These instantaneous properties are different from their corresponding room-temperature values ($H_{k,eff,1}$, $H_{k,eff,2}$, and J_1). The accurate determination of $H'_{k,eff,1}$, $H'_{k,eff,2}$, and J'_1 demands the modeling of the laser heating process as well as the temperature dependence of stack properties, which are challenging. Here, we treat these three variables as adjustable parameters and determine their values by fitting the field-dependent amplitudes of TR-MOKE signals, which yields $H'_{k,eff,1}/H_{k,eff,1} = 0.90 \pm 0.01$, $H'_{k,eff,2}/H_{k,eff,2} = 0.95 \pm 0.01$, and $J'_1/J_1 = 0.83 \pm 0.01$. It is apparent that the field dependence of TR-MOKE signal amplitude is in excellent agreement with the theoretical modeling, as shown in Fig. 4(a).

Figure 4(b) shows the calculated half polar cone angles for each mode in each FM layer. In TR-MOKE signals, the optical mode (the LF mode in regions 2 and 3) tends to be partially canceled out because the two layers precess OOP. Therefore, compared with Fig. 4(a), the information in Fig. 4(b) better reflects the actual intensity of both modes in FM_1 and FM_2. In Fig. 4(b), the precession cone angles of both modes in FM_1 ($\Delta\theta_1^{HF}$, $\Delta\theta_1^{LF}$) have local maxima at the anticrossing field ($H_{ext} \approx 8$ kOe). On the contrary, $\Delta\theta_2^{LF}$ and $\Delta\theta_2^{HF}$ of FM_2 have their maxima either above or below the anticrossing field. This is because FM_2 has larger precession amplitudes (cone angles) than FM_1 at the anticrossing field if there is no IEC [the dotted lines of FM_1 (SL) and FM_2 (SL) in Fig. 4(b)]. With IEC, FM_2 with larger cone angles can drive the precession motion in FM_1 significantly near the anticrossing field, where IEC is effective. Subsequently, the precession amplitudes of FM_1 exhibit local maxima as its cone angle peaks at the anticrossing field [solid lines in Fig. 4(b)]. Also, compared with the uncoupled case [FM_1 (SL) in Fig. 4(b)], FM_1 in the SAF structure has a much larger cone angle at the boundary between regions 1 and 2 ($H_{ext} \approx 1.6$ kOe). This corresponds to the case where FM_1 fast switching is driven by H_{ext}, as shown in Fig. 2(d). The energy valley of FM_1 created by IEC and uniaxial anisotropy is canceled out by H_{ext}. As a result, any perturbation in $H_{k,eff,1}$ or IEC can induce a large change in θ_1.

Besides amplitude, the phase of TR-MOKE signals [β^{HF} and β^{LF} in Eq. (6)] also provides important information about the magnetization dynamics in SAF [Fig. 4(c)]. In Fig. 4(c), the phase of the HF mode stays constant around π. However, the LF mode goes through a π-phase shift at the transition from region 2 to region 3. This phase shift can be explained by the change of the dominant layer from region 2 to region 3 for the LF mode [Fig. 3(c)]. As illustrated in Fig. 4(d), the LF mode (optical mode in regions 2 and 3) has opposite phases in FM_1 ($\sim 0^\circ$) and FM_2 ($\sim 180^\circ$). Considering the two FM layers have comparable optical contributions to TR-MOKE signals ($w \approx 0.5$), TR-MOKE signals will reflect the phase of the dominant layer for each mode. In region 3, FM_2 has larger precession cone angles than FM_1 for the LF mode; therefore, LF TR-MOKE signals have the same phase as FM_2 ($\sim 180^\circ$). However, in region 2, the dominant layer shifts from FM_2 to FM_1 for the LF mode. Hence, the phase of LF TR-MOKE signals also changes by $\sim 180^\circ$ to be consistent with the phase of FM_1 ($\sim 0^\circ$). As for the HF mode, since the two layers always have almost the same phase ($\sim 180^\circ$), the change of the dominant layer does not cause a shift in the phase of TR-MOKE signals.

By comparing Figs. 4(d), 3(a) and 3(b), one can notice that the phase difference between two FM layers could deviate from 0° or 180° when damping and mutual spin pumping is considered [Fig. 4(d)]. The deviation of phase allows energy to be transferred from one FM layer to the other during precession via exchange coupling [54]. In our sample system, FM_2 has a higher damping constant ($\alpha_1 = 0.020$ and $\alpha_2 = 0.060$); therefore, the net transfer of energy is from FM_1 to FM_2. More details can be found in Note 4 of the SM [35], which shows the phase of TR-MOKE signals is affected by Gilbert damping in both layers and the mutual spin pumping. By fitting the phase [Fig. 4(c)] and the damping [Fig. 5(a)] of TR-MOKE signals simultaneously, we obtained $\alpha_{sp,12} = 0.010 \pm 0.004$, and $\alpha_{sp,21} = 0.007^{+0.009}_{-0.007}$, $\alpha_1 = 0.020 \pm 0.002$, and $\alpha_2 = 0.060 \pm 0.008$. Nonreciprocal spin pumping damping ($\alpha_{sp,12} \neq \alpha_{sp,21}$) has been reported in asymmetric FM_1/NM/FM_2 trilayers and attributed to the different spin-mixing conductance ($g_i^{\uparrow\downarrow}$) at the two FM/NM interfaces [27], following $\alpha_{sp,ij} = g_i \mu_B g_j^{\uparrow\downarrow}/(8\pi M_{s,i} d_i)$, with g_i the g factor of the ith layer and μ_B the Bohr magneton [55]. The above equation neglects the spin-flip scattering in NM and assumes that the spin accumulation in the NM spacer equally flows back to FM_1 and FM_2 [37]. However, the uncertainties of our $\alpha_{sp,ij}$ are too high to justify the nonreciprocity of $\alpha_{sp,ij}$ (see Note 3 of the SM [35] for detailed uncertainty analyses). In fact, if the spin backflow to FM_i is proportional to $g_i^{\uparrow\downarrow}$, then $\alpha_{sp,ij} = g_i \mu_B g_i^{\uparrow\downarrow} g_j^{\uparrow\downarrow}/[4\pi M_{s,i} d_i (g_i^{\uparrow\downarrow} + g_j^{\uparrow\downarrow})]$ (Eq. 1.14 in Ref [56]). In this case, the different spin-mixing conductance at two FM/NM interfaces ($g_1^{\uparrow\downarrow} \neq g_2^{\uparrow\downarrow}$) will not lead to nonreciprocal $\alpha_{sp,ij}$. Although differences in g_i and magnetic moment per area ($M_{s,i} d_i$) can potentially lead to nonreciprocal $\alpha_{sp,ij}$, the values of g_i and $M_{s,i} d_i$ for the two FM layers are expected to be similar (the net magnetization of SAF is zero without external fields). Therefore, nearly reciprocal $\alpha_{sp,ij}$ are plausible for our SAF stack. Assuming $g_i^{\uparrow\downarrow}$ values are similar at the two FM/NM interfaces ($g_1^{\uparrow\downarrow} \approx g_2^{\uparrow\downarrow} = g^{\uparrow\downarrow}$), this yields $g^{\uparrow\downarrow} = 8\pi M_{s,i} d_i \alpha_{sp,ij}/(g_i \mu_B) = 1.2 \sim 1.7 \times 10^{15}\,\mathrm{cm}^{-2}$. $g^{\uparrow\downarrow}$ can also be estimated from the free electron density per spin (n) in the NM layer: $g^{\uparrow\downarrow} \approx 1.2 n^{2/3}$ [57]. With $n = 5.2 \times 10^{28}\,\mathrm{m}^{-3}$ for Ru [58] (the value of n is similar for Ta [59]), $g^{\uparrow\downarrow}$ is estimated to be $1.7 \times 10^{15}\,\mathrm{cm}^{-2}$, the same order as the $g^{\uparrow\downarrow}$ value from TR-MOKE measurements, which justifies the $\alpha_{sp,ij}$ values derived from TR-MOKE are within a reasonable range. The values of α_1 and α_2 will be discussed in Sec. III D.

D. Magnetic damping of the HF and LF precession modes

In addition to the amplitude and phase of TR-MOKE signals for the p-SAF stack, the model analyses also provide a better understanding of magnetic damping. Figure 5(a) shows the effective damping constant ($\alpha_{eff} = 1/2\pi f \tau$) measured at different H_{ext} (symbols), in comparison with modeling fitting (solid lines). The general H_{ext} dependence of α_{eff} can be well captured by the model. The fitted Gilbert

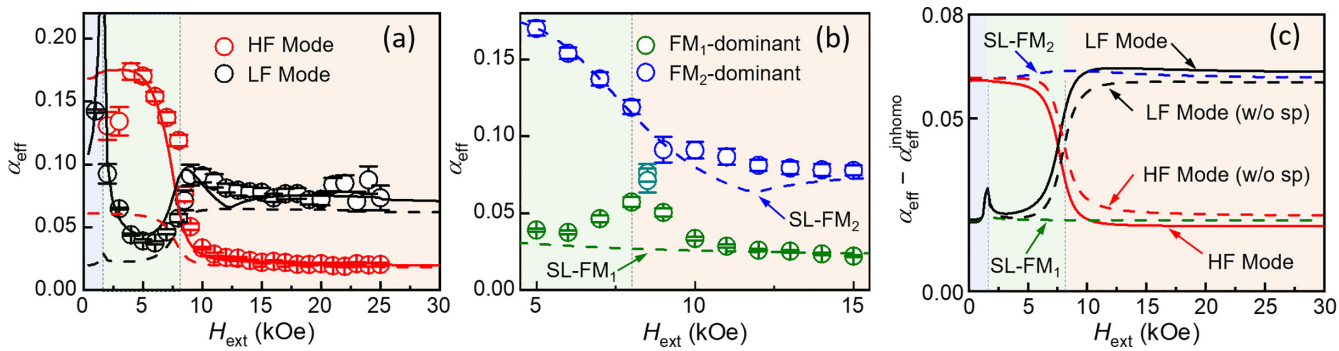

FIG. 5. (a) Effective damping constant under varying H_{ext}. Circles are experimental data. Solid lines are fitting curves based on Eqs. (4) and (5). Dashed lines denote α_{eff} after the removal of inhomogeneous-broadening contribution. (b) A zoomed-in figure of (a) between 5 and 15 kOe. Blue and green circles are measured effective damping of the mode dominated by FM_1 and FM_2, respectively. Blue and green dashed lines are the α_{eff} of FM_1 and FM_2 single layer without IEC. (c) Effective damping after excluding the inhomogeneous contribution as a function of H_{ext}. The HF mode (red curves) and the LF mode (black curves) are represented by solid (or dashed) curves when the mutual spin pumping terms ($\alpha_{sp,12}$ and $\alpha_{sp,21}$) are considered (or excluded). The dashed green and blue lines are the SL cases for FM_1 and FM_2, respectively.

damping, $\alpha_1 = 0.020 \pm 0.002$ and $\alpha_2 = 0.060 \pm 0.008$ are close to the Gilbert damping of Ta/CoFeB(1 nm)/MgO thin films (∼0.017) [41,60] and Co/Pd multilayers with a similar t_{Co}/t_{Pd} ratio (∼0.085) [61]. Other fitted parameters are $\Delta H_{k,eff,1} = 0.26 \pm 0.02$ kOe, $\Delta H_{k,eff,2} = 1.42 \pm 0.18$ kOe, $\alpha_{12}^{sp} = 0.010 \pm 0.004$, and $\alpha_{21}^{sp} = 0.007^{+0.009}_{-0.007}$. ΔJ_1 and ΔJ_2 are set to be zero, as explained in Sec. II B. More details regarding the values and determination methods of all parameters involved in our data reduction are provided in Note 3 of the SM [35]. The dashed lines show the calculated α_{eff} without inhomogeneous broadening. At high H_{ext}, the difference between the solid lines and dashed lines approaches zero because the inhomogeneous broadening is suppressed. At low H_{ext}, the solid lines are significantly higher than the dashed lines, indicating substantial inhomogeneous broadening contributions.

The effective damping shows interesting features near the anticrossing field. As shown in Fig. 5(b), due to the effective coupling between two FM layers near the anticrossing field, the hybridization of precession in two FM layers leads to a mix of damping with contributions from both layers. The effective damping of the FM_1-dominant mode reaches a maximum within the anticrossing region ($7 \leqslant H_{ext} \leqslant 10$ kOe) and is higher than the single-layer (SL) FM_1 case. Similarly, the hybridized HF and LF modes at 8.5 kOe exhibit a lower α_{eff} (∼0.073) compared to the SL FM_2 case. α_{eff} consists of contributions from Gilbert damping (α_i), mutual spin pumping ($\alpha_{sp,ij}$, $i \neq j$), and inhomogeneous broadening ($\Delta H_{k,eff,i}$ and ΔJ_i). To better understand the mixing damping behavior, Fig. 5(c) shows α_{eff} after excluding the inhomogeneous contribution (α_{eff}^{inhomo}). Compared to the SL layer case (green and blue dashed lines), the HF and LF modes (red and black dashed lines) clearly suggest that IEC effectively mixes the damping in two layers around the anticrossing field. Without the IEC, precession in FM_2 with a higher damping relaxes faster than that in FM_1. However, the IEC provides a channel to transfer energy from FM_1 to FM_2, such that the two layers have the same precession relaxation rate for a given mode. Near the anticrossing field, two layers have comparable precession cone angles; therefore, the damping values of the hybridized modes are roughly the average of two FM layers. In addition to the static IEC, dynamic spin pumping can also modify the damping of individual modes. The black and red solid lines represent the cases with mutual spin pumping ($\alpha_{sp,12} = 0.01$ and $\alpha_{sp,21} = 0.007$). Generally, in regions 2 and 3, mutual spin pumping reduces the damping of the HF mode and increases the damping of the LF mode because the HF (LF) mode is near IP (OOP). Overall, the static IEC still plays the essential role for the damping mix near the anticrossing field.

IV. CONCLUSION

We systematically investigated the magnetization dynamics excited by ultrafast laser pulses in an asymmetric p-SAF sample both theoretically and experimentally. We obtained detailed information regarding magnetization dynamics, including the cone angles, directions, and phases of spin precession in each layer under different H_{ext}. In particular, the dynamic features in the low-field region (region 1) exhibiting CW precession, were revealed. The resonance between the precession of two FM layers occurs at the boundary between regions 2 and 3, where an anticrossing feature is present in the frequency vs H_{ext} profile. The dominant FM layer for a given precession mode also switches from region 2 to region 3. The amplitude and phase of TR-MOKE signals are well captured by theoretical modeling. Importantly, we successfully quantified the individual contributions from various sources to the effective damping, which enables the determination of Gilbert damping for both FM layers. At low H_{ext}, the contribution of inhomogeneous broadening to the effective damping is significant. Near the anticrossing field, the effective damping of two coupled modes contains substantial contributions from both FM layers owing to the strong hybridization via IEC. Although the analyses were made for an asymmetric SAF sample, this approach can be directly applied to study magnetization dynamics and magnetic properties of general complex material systems with coupled multilayers, and thus benefits the design and optimization of spintronic materials via structural engineering.

ACKNOWLEDGMENTS

This work is primarily supported by the National Science Foundation (NSF, CBET-2226579). D.L.Z gratefully acknowledges the funding support from the ERI program (FRANC) "Advanced MTJs for computation in and near random access memory" by DARPA, and ASCENT, one of six centers in JUMP (a Semiconductor Research Corporation program, sponsored by MARCO and DARPA). J.P.W and X.J.W also appreciate the partial support from the UMN MRSEC Seed program (NSF, DMR-2011401). D.B.H. acknowledges the support from the UMN 2022–2023 Doctoral Dissertation Fellowship. The authors appreciate the valuable discussion with Professor P. Crowell.

[1] R. Chen, Q. Cui, L. Liao, Y. Zhu, R. Zhang, H. Bai, Y. Zhou, G. Xing, F. Pan, H. Yang *et al.*, Reducing Dzyaloshinskii-Moriya interaction and field-free spin-orbit torque switching in synthetic antiferromagnets, Nat. Commun. **12**, 3113 (2021).

[2] W. Legrand, D. Maccariello, F. Ajejas, S. Collin, A. Vecchiola, K. Bouzehouane, N. Reyren, V. Cros, and A. Fert, Room-temperature stabilization of antiferromagnetic skyrmions in synthetic antiferromagnets, Nat. Mater. **19**, 34 (2020).

[3] D.-L. Zhang, C. Sun, Y. Lv, K. B. Schliep, Z. Zhao, J.-Y. Chen, P. M. Voyles, and J.-P. Wang, $L1_0$ Fe-Pd Synthetic Antiferromagnet Through an fcc Ru Spacer Utilized for Perpendicular Magnetic Tunnel Junctions, Phys. Rev. Appl. **9**, 044028 (2018).

[4] D.-S. Han, K. Lee, J.-P. Hanke, Y. Mokrousov, K.-W. Kim, W. Yoo, Y. L. W. van Hees, T.-W. Kim, R. Lavrijsen, C.-Y. You *et al.*, Long-range chiral exchange interaction in synthetic antiferromagnets, Nat. Mater. **18**, 703 (2019).

[5] S.-H. Yang, K.-S. Ryu, and S. Parkin, Domain-wall velocities of up to 750 m s^{-1} driven by exchange-coupling torque in synthetic antiferromagnets, Nat. Nanotechnol. **10**, 221 (2015).

[6] A. Fernández-Pacheco, E. Vedmedenko, F. Ummelen, R. Mansell, D. Petit, and R. P. Cowburn, Symmetry-breaking interlayer Dzyaloshinskii-Moriya interactions in synthetic antiferromagnets, Nat. Mater. **18**, 679 (2019).

[7] T. Moriyama, W. Zhou, T. Seki, K. Takanashi, and T. Ono, Spin-Orbit-Torque Memory Operation of Synthetic Antiferromagnets, Phys. Rev. Lett. **121**, 167202 (2018).

[8] R. A. Duine, K.-J. Lee, S. S. P. Parkin, and M. D. Stiles, Synthetic antiferromagnetic spintronics, Nat. Phys. **14**, 217 (2018).

[9] S. Yang, T.-S. Ju, J. Seo, K.-W. Moon, C. Kim, H.-J. Kim, J. Shin, J. Yang, C. Hwang, and J. Hong, Ultralow-current magnetization switching in nearly compensated synthetic antiferromagnetic frames using sandwiched spin sources, Acta Mater. **208**, 116708 (2021).

[10] S. Bandiera, R. C. Sousa, Y. Dahmane, C. Ducruet, C. Portemont, V. Baltz, S. Auffret, I. L. Prejbeanu, and B. Dieny, Comparison of synthetic antiferromagnets and hard ferromagnets as reference layer in magnetic tunnel junctions with perpendicular magnetic anisotropy, IEEE Magn. Lett. **1**, 3000204 (2010).

[11] C.-Y. You, Effect of the synthetic antiferromagnetic polarizer layer rigidness on the spin transfer torque switching current density, Appl. Phys. Lett. **103**, 042402 (2013).

[12] D. Houssameddine, J. F. Sierra, D. Gusakova, B. Delaet, U. Ebels, L. D. Buda-Prejbeanu, M. C. Cyrille, B. Dieny, B. Ocker, J. Langer *et al.*, Spin torque driven excitations in a synthetic antiferromagnet, Appl. Phys. Lett. **96**, 072511 (2010).

[13] Y. Shiota, T. Taniguchi, M. Ishibashi, T. Moriyama, and T. Ono, Tunable Magnon-Magnon Coupling Mediated by Dynamic Dipolar Interaction in Synthetic Antiferromagnets, Phys. Rev. Lett. **125**, 017203 (2020).

[14] A. Bergman, B. Skubic, J. Hellsvik, L. Nordström, A. Delin, and O. Eriksson, Ultrafast switching in a synthetic antiferromagnetic magnetic random-access memory device, Phys. Rev. B **83**, 224429 (2011).

[15] D. Lyu, D. Zhang, D. B. Gopman, Y. Lv, O. J. Benally, and J.-P. Wang, Ferromagnetic resonance and magnetization switching characteristics of perpendicular magnetic tunnel junctions with synthetic antiferromagnetic free layers, Appl. Phys. Lett. **120**, 012404 (2022).

[16] D. Lyu, J. E. Shoup, D. Huang, J. García-Barriocanal, Q. Jia, W. Echtenkamp, G. A. Rojas, G. Yu, B. R. Zink, X. Wang *et al.*, Sputtered $L1_0$-FePd and its synthetic antiferromagnet on Si/SiO_2 wafers for scalable spintronics, Adv. Funct. Mater. **33**, 2214201 (2023).

[17] B. Heinrich, G. Woltersdorf, R. Urban, and E. Simanek, Role of dynamic exchange coupling in magnetic relaxations of metallic multilayer films (invited), J. Appl. Phys. **93**, 7545 (2003).

[18] A. J. Annunziata, P. L. Trouilloud, S. Bandiera, S. L. Brown, E. Gapihan, E. J. O'Sullivan, and D. C. Worledge, Materials investigation for thermally-assisted magnetic random access memory robust against 400 °C temperatures, J. Appl. Phys. **117**, 17B739 (2015).

[19] H. Yang, Y. Li, and W. E. Bailey, Large spin pumping effect in antisymmetric precession of $Ni_{79}Fe_{21}/Ru/Ni_{79}Fe_{21}$, Appl. Phys. Lett. **108**, 242404 (2016).

[20] K. Tanaka, T. Moriyama, M. Nagata, T. Seki, K. Takanashi, S. Takahashi, and T. Ono, Linewidth broadening of optical precession mode in synthetic antiferromagnet, Appl. Phys. Express **7**, 063010 (2014).

[21] S. Sorokin, R. A. Gallardo, C. Fowley, K. Lenz, A. Titova, G. Y. P. Atcheson, G. Dennehy, K. Rode, J. Fassbender, J. Lindner *et al.*, Magnetization dynamics in synthetic antiferromagnets: Role of dynamical energy and mutual spin pumping, Phys. Rev. B **101**, 144410 (2020).

[22] A. Kamimaki, S. Iihama, T. Taniguchi, and S. Mizukami, All-optical detection and evaluation of magnetic damping in synthetic antiferromagnet, Appl. Phys. Lett. **115**, 132402 (2019).

[23] G. Wu, S. Chen, Y. Ren, Q. Y. Jin, and Z. Zhang, Laser-induced magnetization dynamics in interlayer-coupled $[Ni/Co]_4/Ru/[Co/Ni]_3$ perpendicular magnetic films for information storage, ACS Appl. Nano Mater. **2**, 5140 (2019).

[24] G. Wu, S. Chen, S. Lou, Y. Liu, Q. Y. Jin, and Z. Zhang, Annealing effect on laser-induced magnetization dynamics in Co/Ni-based synthetic antiferromagnets with perpendicular magnetic anisotropy, Appl. Phys. Lett. **115**, 142402 (2019).

[25] G. Wu, W. Zhu, Z. Zhu, H. Xue, Y. Ren, Y. Liu, Q. Y. Jin, and Z. Zhang, Magnetic precession modes with enhanced frequency and intensity in hard/NM/soft perpendicular magnetic films, Phys. Chem. Chem. Phys. **21**, 16830 (2019).

[26] S. Mangin, D. Ravelosona, J. A. Katine, M. J. Carey, B. D. Terris, and E. E. Fullerton, Current-induced magnetization reversal in nanopillars with perpendicular anisotropy, Nat. Mater. **5**, 210 (2006).

[27] Y. Pogoryelov, M. Pereiro, S. Jana, A. Kumar, S. Akansel, M. Ranjbar, D. Thonig, D. Primetzhofer, P. Svedlindh, J. Åkerman *et al.*, Nonreciprocal spin pumping damping in asymmetric magnetic trilayers, Phys. Rev. B **101**, 054401 (2020).

[28] T. Chiba, G. E. W. Bauer, and S. Takahashi, Magnetization damping in noncollinear spin valves with antiferromagnetic interlayer couplings, Phys. Rev. B **92**, 054407 (2015).

[29] Y. Zhang, G. Wu, Z. Ji, X. Chen, Q. Y. Jin, and Z. Zhang, Significant and Nonmonotonic Dynamic Magnetic Damping in Asymmetric Co-Fe/Ru/Co-Fe Trilayers, Phys. Rev. Appl. **17**, 034033 (2022).

[30] D. Huang, D. Lattery, and X. Wang, Materials engineering enabled by time-resolved magneto-optical Kerr effect for spintronic applications, ACS Appl. Electron. Mater. **3**, 119 (2021).

[31] D. M. Lattery, J. Zhu, D. Huang, and X. Wang, Ultrafast thermal and magnetic characterization of materials enabled by the time-resolved magneto-optical Kerr effect, in *Nanoscale Energy Transport: Emerging Phenomena, Methods and Applications*, edited by B. Liao (IOP Publishing, London, 2020), p. 9.

[32] D. M. Lattery, D. Zhang, J. Zhu, X. Hang, J. P. Wang, and X. Wang, Low Gilbert damping constant in perpendicularly magnetized W/CoFeB/MgO films with high thermal stability, Sci. Rep. **8**, 13395 (2018).

[33] D. Huang, D. Lyu, X. Wang, M. B. Katz, D. Zhang, J.-P. Wang, D. B. Gopman, and X. Wang, Temperature-dependent perpendicular anisotropy and Gilbert damping of $L1_0$-FePd films: Role of noble-metal buffer layers, Phys. Rev. Mater. **6**, 113402 (2022).

[34] P. J. H. Bloemen, H. W. Van Kesteren, H. J. M. Swagten, and W. J. M. De Jonge, Oscillatory interlayer exchange coupling in Co/Ru multilayers and bilayers, Phys. Rev. B **50**, 13505 (1994).

[35] See Supplemental Material at http://link.aps.org/supplemental/10.1103/PhysRevB.107.214438 for the analyses of the magnetization precession in each ferromagnetic layer; the estimation of each layer's contribution to total TR-MOKE signals; a summary of the parameters and uncertainties used in the data reduction; the impacts of α_1, α_2, and mutual spin pumping on phase; and the region diagrams for p-SAF with different degrees of asymmetries.

[36] Z. Zhang, L. Zhou, P. E. Wigen, and K. Ounadjela, Angular dependence of ferromagnetic resonance in exchange-coupled Co/Ru/Co trilayer structures, Phys. Rev. B **50**, 6094 (1994).

[37] B. Heinrich, Y. Tserkovnyak, G. Woltersdorf, A. Brataas, R. Urban, and G. E. W. Bauer, Dynamic Exchange Coupling in Magnetic Bilayers, Phys. Rev. Lett. **90**, 187601 (2003).

[38] A. Brataas, Y. Tserkovnyak, G. E. W. Bauer, and B. I. Halperin, Spin battery operated by ferromagnetic resonance, Phys. Rev. B **66**, 060404(R) (2002).

[39] Y. Tserkovnyak, A. Brataas, and G. E. W. Bauer, Spin pumping and magnetization dynamics in metallic multilayers, Phys. Rev. B **66**, 224403 (2002).

[40] Y. Tserkovnyak, A. Brataas, and G. E. W. Bauer, Enhanced Gilbert Damping in Thin Ferromagnetic Films, Phys. Rev. Lett. **88**, 117601 (2002).

[41] S. Iihama, S. Mizukami, H. Naganuma, M. Oogane, Y. Ando, and T. Miyazaki, Gilbert damping constants of Ta/CoFeB/MgO(Ta) thin films measured by optical detection of precessional magnetization dynamics, Phys. Rev. B **89**, 174416 (2014).

[42] D. Zhang, D. Huang, R. J. Wu, D. Lattery, J. Liu, X. Wang, D. B. Gopman, K. A. Mkhoyan, J.-P. Wang, and X. Wang, Low Gilbert damping and high thermal stability of Ru-seeded $L1_0$-phase FePd perpendicular magnetic thin films at elevated temperatures, Appl. Phys. Lett. **117**, 082405 (2020).

[43] J. C. Slonczewski, Overview of interlayer exchange theory, J. Magn. Magn. Mater. **150**, 13 (1995).

[44] J. C. Slonczewski, Fluctuation Mechanism for Biquadratic Exchange Coupling in Magnetic Multilayers, Phys. Rev. Lett. **67**, 3172 (1991).

[45] W. Wang, P. Li, C. Cao, F. Liu, R. Tang, G. Chai, and C. Jiang, Temperature dependence of interlayer exchange coupling and Gilbert damping in synthetic antiferromagnetic trilayers investigated using broadband ferromagnetic resonance, Appl. Phys. Lett. **113**, 042401 (2018).

[46] A. Kundu and S. Zhang, Temperature dependence of RKKY interaction, J. Magn. Magn. Mater. **393**, 331 (2015).

[47] C. Y. You and S. C. Shin, Generalized analytic formulae for magneto-optical Kerr effects, J. Appl. Phys. **84**, 541 (1998).

[48] A. J. Schellekens, K. C. Kuiper, R. R. J. C. de Wit, and B. Koopmans, Ultrafast spin-transfer torque driven by femtosecond pulsed-laser excitation, Nat. Commun. **5**, 4333 (2014).

[49] B. Koopmans, G. Malinowski, F. Dalla Longa, D. Steiauf, M. Fähnle, T. Roth, M. Cinchetti, and M. Aeschlimann, Explaining the paradoxical diversity of ultrafast laser-induced demagnetization, Nat. Mater. **9**, 259 (2010).

[50] G. Malinowski, F. Dalla Longa, J. H. H. Rietjens, P. V. Paluskar, R. Huijink, H. J. M. Swagten, and B. Koopmans, Control of speed and efficiency of ultrafast demagnetization by direct transfer of spin angular momentum, Nat. Phys. **4**, 855 (2008).

[51] D. M. Lattery, J. Zhu, D. Zhang, J. P. Wang, P. A. Crowell, and X. Wang, Quantitative analysis and optimization of magnetization precession initiated by ultrafast optical pulses, Appl. Phys. Lett. **113**, 162405 (2018).

[52] T. M. J. Cham, S. Karimeddiny, A. H. Dismukes, X. Roy, D. C. Ralph, and Y. K. Luo, Anisotropic gigahertz antiferromagnetic resonances of the easy-axis van der Waals antiferromagnet CrSBr, Nano Lett. **22**, 6716 (2022).

[53] Y. Shiota, T. Arakawa, R. Hisatomi, T. Moriyama, and T. Ono, Polarization-Selective Excitation of Antiferromagnetic Resonance in Perpendicularly Magnetized Synthetic Antiferromagnets, Phys. Rev. Appl. **18**, 014032 (2022).

[54] D. H. Zanette, Energy exchange between coupled mechanical oscillators: Linear regimes, J. Phys. Commun. **2**, 095015 (2018).

[55] C. J. Durrant, L. R. Shelford, R. A. J. Valkass, R. J. Hicken, A. I. Figueroa, A. A. Baker, G. van der Laan, L. B. Duffy, P. Shafer, C. Klewe *et al.*, Dependence of spin pumping and spin transfer torque upon $Ni_{81}Fe_{19}$ thickness in

Ta/Ag/$Ni_{81}Fe_{19}$/Ag/Co_2MnGe/Ag/Ta spin-valve structures, Phys. Rev. B **96**, 144421 (2017).

[56] Y. Tserkovnyak, Spin and charge transfer in selected nanostructures, Ph.D. thesis, Harvard University, 2003.

[57] B. Kardasz and B. Heinrich, Ferromagnetic resonance studies of accumulation and diffusion of spin momentum density in Fe/Ag/Fe/GaAs(001) and Ag/Fe/GaAs(001) structures, Phys. Rev. B **81**, 094409 (2010).

[58] Y. Petrov, K. Migdal, N. Inogamov, V. Khokhlov, D. Ilnitsky, I. Milov, N. Medvedev, V. Lipp, and V. Zhakhovsky, Ruthenium under ultrafast laser excitation: Model and dataset for equation of state, conductivity, and electron-ion coupling, Data in Brief **28**, 104980 (2020).

[59] A. Dabral, G. Pourtois, K. Sankaran, W. Magnus, H. Yu, A. de Jamblinne de Meux, A. K. A. Lu, S. Clima, K. Stokbro, M. Schaekers *et al.*, Study of the intrinsic limitations of the contact resistance of metal/semiconductor interfaces through atomistic simulations, ECS J. Solid State Sci. Technol. **7**, N73 (2018).

[60] B. Liu, D. Huang, M. Gao, H. Tu, K. Wang, X. Ruan, J. Du, J.-W. Cai, L. He, J. Wu *et al.*, The effect of growth sequence on magnetization damping in Ta/CoFeB/MgO structures, J. Magn. Magn. Mater. **450**, 65 (2018).

[61] T. Kato, Y. Matsumoto, S. Kashima, S. Okamoto, N. Kikuchi, S. Iwata, O. Kitakami, and S. Tsunashima, Perpendicular anisotropy and Gilbert damping in sputtered Co/Pd multilayers, IEEE Trans. Magn. **48**, 3288 (2012).